Separation and Purification Technology 371 (2025) 133100

Contents lists available at ScienceDirect

Separation and Purification Technology

journal homepage: www.elsevier.com/locate/seppur

A mechanistic process model for aqueous two-phase flotation: Insights into enzyme transport mechanisms

Kim Carina Lohfink, Hermann Nirschl, Frank Rhein *

Institute of Mechanical Process Engineering and Mechanics, Karlsruhe Institute of Technology (KIT), Strasse am Forum 8, Karlsruhe, 76131, Germany

ARTICLE INFO

Communicated by Raquel Aires Barros

Dataset link: KITopen / Radar, pdhs-group/ATPF

Keywords:
Aqueous two-phase flotation (ATPF)
Enzyme separation
Compartment model
Mass transfer

ABSTRACT

Continuous aqueous two-phase flotation (ATPF) is an alternative downstream approach for the selective separation of enzymes from complex biosuspensions. Until now, mass transport across the phase interface has been assumed to be mainly due to accumulation of enzymes on the surface of rising gas bubbles (flotation), while theoretical studies are lacking. This work presents a mechanistic compartment model of the ATPF process that also includes mass transport by extraction, i.e. diffusion across the phase interface. The model is validated with ATPF experiments over a wide range of process parameters and reliably predicts the process behavior. The results indicate that extraction accounts for more than 80% of the integral mass transfer, while bubbles are still essential for phase mixing and the creation of a large interfacial area. Therefore, the proposed process model provides valuable insights into the enzyme transport mechanisms and enables future developments such as model predictive control.

1. Introduction

The biotechnology industry has undergone significant expansion in recent years. Enzymes, in particular, are becoming increasingly important for use in industrial processes. Operating as biological catalysts, enzymes find application in a broad spectrum of sectors, including food and beverages, pharmaceuticals, paper production, cosmetics, and biofuels [1,2]. The substitution of conventional chemical catalysis processes ensures enhanced sustainability and a reduction of environmental impact. They are biodegradable and catalyze reactions efficiently and selectively, improving product quality and reducing costs [1,2].

Most enzyme applications require a high degree of purity. Therefore, a complex downstream process is necessary to separate and recover the product after biosynthesis. Due to the large number of unit operations for separation and concentration (e.g. centrifugation, ultrafiltration) inherent in downstream processing of enzymes is associated with substantial energy and chemical costs [3,4]. As an effective and environmentally friendly alternative to conventional enzyme recovery, aqueous two-phase flotation (ATPF) was proposed by Bi et al. [5] in 2009. The basis for ATPF is an aqueous two-phase system (ATPS) created by mixing the phase-forming components above critical concentrations. The resulting system comprises two coexisting, immiscible phases that differ in both density and hydrophobicity. Typically, two polymers (polymer/polymer-ATPS) or a polymer and a salt (polymer/salt-ATPS) are employed as phase-forming components [4,6]. The polymer-rich, low density top phase is then layered on top. The high water content of both phases in excess of 80% ensures that ATPF provides a mild environment for sensitive biomolecules.

In contrast to aqueous two-phase extraction (ATPE), gas bubbles are introduced to the bottom of the ATPS through suitable porous media (e.g. twill weave, glass membrane). The biomolecules present in the bottom phase attach their hydrophobic regions to the bubble surfaces and are transported vertically upwards by the bubble. The molecules are released into the top phase as the bubble passes through the top phase and then bursts on the top phase/atmosphere interface [4,7]. The low volume ratio of top to bottom phase, typically 0.03 to 0.25, further increases the concentration factor of the process. This also results in a reduction in the consumption of top phase chemicals, leading to a more environmentally friendly process [4,8]. The application of ATPF has been extensively documented in the separation and recovery of a wide range of biomolecules [5,7,9–18].

Although ATPF has already been extensively researched for various products, ATPS and process optimization [4,19–21], there is a lack of theoretical research in the field of ATPF. This concerns a process model as well as kinetic and thermodynamic considerations [4]. For the application of ATPF on an industrial scale, automated control is advantageous. In order to develop a feedback controller for the ATPF process, a reliable prediction of the system behavior is crucial [22]. A mechanistic process model considers physical and empirical correlations occurring in the respective process, in particular the mass

* Corresponding author.
E-mail address: frank.rhein@kit.edu (F. Rhein).

https://doi.org/10.1016/j.seppur.2025.133100
Received 17 March 2025; Received in revised form 16 April 2025; Accepted 17 April 2025
Available online 3 May 2025

Table 1
Composition of the aqueous two-phase system (ATPS).

Phase	x_{PEG}/% (w/w)	$x_{citrate}$/% (w/w)	x_{enzyme}/% (w/w)
top	39.45	2.97	0.00
bottom	0.66	25.78	1.00 – 4.00

transport mechanisms. Up to now, it has been assumed that mass transport occurs mainly by accumulation of biomolecules on the bubble surfaces (flotation). Diffusive molecular mass transport provides an additional transfer of the target molecules from the bottom phase to the top phase (extraction). This second mass transport mechanism is driven by differences in the concentration and hydrophobicity of the two aqueous phases [4]. It has been considered negligible due to the small liquid/liquid interface, however, gas bubbles can generate a zone of phase mixing, where the interfacial area is larger and extraction, i.e. ATPE can occur.

This work develops a mechanistic process model for ATPF by discretizing the process volume into compartments. For each compartment, a mass balance equation is solved to describe the local molar enzyme concentration over time. The model considers the mass transport phenomena of convection (horizontal mass transport by phase exchange), flotation (vertical mass transport by accumulation at rising bubbles), and extraction (vertical mass transport by diffusion across the phase interface). Each transport mechanism is discussed and modeled based on simplifying assumptions. This results in two empirical model parameters, which are optimized based on experimental data obtained from a laboratory ATPF plant with integrated online measurement technology, as previously proposed in [21]. In addition to enabling model predictive control (MPC), the model provides valuable insights into the micro processes of ATPF: This work closes with a thorough discussion on the relevance of the individual mass transport phenomena, thus contributing significantly to the general understanding and development of ATPF.

2. Materials & methods

2.1. Continuous ATPF experiments

2.1.1. Aqueous two-phase system (ATPS)

A polymer/salt ATPS was used for ATPF experiments. The phase-forming components were polyethylene glycol (PEG) 1000 (Ph. Eur., Carl Roth GmbH + Co. KG, Karlsruhe, Germany) and trisodium citrate dihydrate (Ph. Eur., Carl Roth GmbH + Co. KG, Karlsruhe, Germany). The concentrations x_i of the phase-forming components of the polymer-rich top phase (top) and the salt-rich bottom phase (bot) are given in Table 1. Demineralized water was used for phase preparation. Phospholipase A_2 (PLP 21159, Sternenzym GmbH + Co. KG, Ahrensburg, Germany) was used as the model enzyme and was added to the bottom phase at concentrations between 1.00% (w/w) and 4.00% (w/w).

2.1.2. Laboratory ATPF plant with integrated online measurement technology

The laboratory setup presented in [21] was used to generate experimental data. A photo is shown in Fig. 1(a). The polymer-salt ATPS (see Section 2.1.1) is placed in the flotation tank. Two peristaltic pumps (Ismatec Reglo ICC, Cole Parmer, St. Neots, UK) were used to control the flow rates of top and bottom phase. The flotation tank was equipped with three gassing units, which introduce air bubbles into the bottom phase through twill weaves (nominal pore size 10 µm, TopMesh TM10, Spoerl, Sigmaringendorf, Germany). Three mass flow controllers (SLA55800, Brooks Instrument, Dresden, Germany) were used to separately control the gas flow rates.

To determine the separation efficiency and the phase mixing during the experiments, online measurement technology was integrated into the system. The real-time measurement of the enzyme concentration at the outlet was performed by UV/Vis spectroscopy (HR-4UVV250-25, Ocean Optics B.B., Ostfildern, Germany). The sample leaving the flotation tank passed through the flow cell of the UV/Vis spectrometer where the absorbance of the sample in the UV/Vis wavelength range was determined. Since the enzyme used, like all proteins, is composed of amino acids, it has a peak at 280 nm in the UV/Vis spectrum [23]. According to the Beer–Lambert law, the height of the peak correlates linearly with the enzyme concentration in the sample [24]. Therefore, the enzyme concentration was determined by calibration from the measured absorbance at 28 nm. Three electrical conductivity probes were integrated into the plant for spatially resolved determination of phase mixing. These probes were positioned horizontally offset from the gassing units and 1 cm below the phase interface, a configuration that mitigates the effect of gas bubbles on the measured values. The calculation of phase mixing is based on the significantly different electrical conductivities of the two phases due to their different salt content. High phase mixing results in reduced measured electrical conductivities, as the bottom phase is increasingly displaced from the conductivity probes by the top phase [20].

LabVIEW (version 21.1.2, National Instruments, Austin, Texas, USA) was used as the central process control software. This software was used to configure the flow rates of the peristaltic pumps and the mass flow controllers, and to read and store data from the UV/Vis spectrometer and electrical conductivity probes in real-time during the experiments.

2.1.3. Experimental procedure

In order to calibrate and validate the ATPF process model, measurements from the UV/Vis spectrometer and electrical conductivity probes from ATPF experiments with different process parameters (i.e., volume flows of the three gassing units and the peristaltic pumps for top phase and bottom phase) are required. A run table of all performed experiments and their respective parameter settings is provided in SI Table C.1. Before starting the ATPF experiment, 500 mL of bottom phase, loaded with the model enzyme, was added to the flotation tank. Using the top phase peristaltic pump, 100 mL of unloaded top phase was carefully added on top. The experiment started as soon as the three mass flow controllers and the peristaltic pumps were turned on simultaneously using LabVIEW (see Section 2.1.2). At the same time, LabVIEW began recording and storing data from the UV/Vis spectrometer and the three conductivity probes in a one minute interval. All continuous ATPF experiments in this work were performed with constant process parameters.

2.2. Continuous ATPF model development

2.2.1. Compartment model for the local enzyme concentration

Fig. 1(b) shows a schematic representation of the ATPF basin. Vertically, the volume is split into two sections, the top phase (`[0,:]`) and the bottom (bot) phase (`[1,:]`). Horizontally, each phase is discretized according to the three gas inlets. In both the top and bottom phase, all horizontal compartments are of equal volume, i.e. $V(0,0) = V(0,1) = V(0,2) = V_{top,total}/3$ and $V(1,0) = V(1,1) = V(1,2) = V_{bot,total}/3$. The volume flow rates of the top ($\dot{Q}_{top}$) and bottom ($\dot{Q}_{bot}$) phase, as well as their molar enzyme concentrations $c_{0,bot}$ and $c_{0,top}$ are constant for each experiment. Each compartment is assumed to be perfectly mixed, i.e. spatially homogeneous. Furthermore, no volumetric flow is assumed between the bottom and the top phase and all compartment volumes $V(i,j)$ are assumed to be constant, i.e. the volumetric flows entering from the left exit to the right without accumulation. Three enzyme transport mechanism are shown in Fig. 1 with their corresponding molar flow rates $\dot{M}$: Convective transport via the horizontal flow $\dot{M}_c$, transport via the surface of the bubbles (flotation) $\dot{M}_f$ and transport across the top/bottom interface due to concentration gradients (extraction) $\dot{M}_e$. The mass balance for compartment (i,j)

$$V(i,j)\frac{dc(i,j,t)}{dt} = \underbrace{\dot{M}_{c,in}(i,j,t) - \dot{M}_{c,out}(i,j,t)}_{\text{convection}} + \underbrace{\dot{M}_f(i,j,t)}_{\text{flotation}} + \underbrace{\dot{M}_e(i,j,t)}_{\text{extraction}} \quad (1)$$

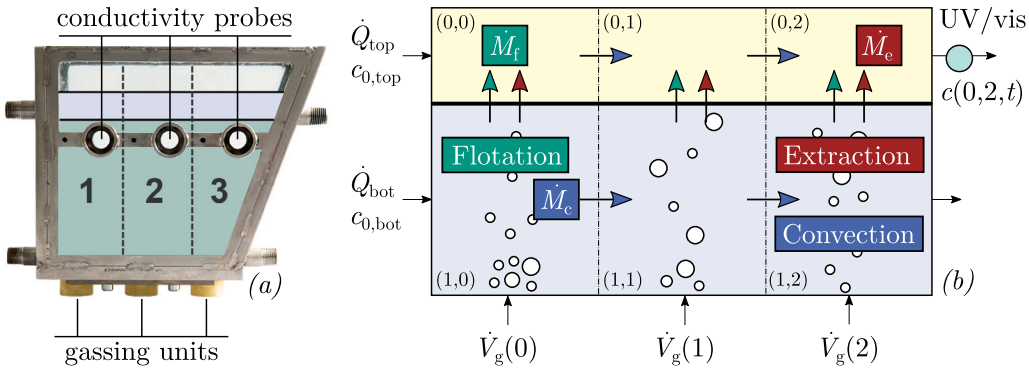

Fig. 1. Photograph (a) and compartment model scheme (b) of the ATPF process. The relevant transport mechanisms are indicated by color and arrows, while variable names are introduced in the main text.

describes how the molar concentration changes with time.

Assuming spatially homogeneous compartments and only horizontal flow, the convective term is defined as

$$\dot{M}_{c,in}(i,j,t) - \dot{M}_{c,out}(i,j,t) = (c(i,j-1,t) - c(i,j,t))\,\dot{Q}(i) \quad . \tag{2}$$

Gas is introduced on the bottom of all three bottom compartments with individual gas flow rates $\dot{V}_g(0)$, $\dot{V}_g(1)$ and $\dot{V}_g(2)$ at constant pressure. Gas passes through the bottom phase, collects enzyme and passes the top/bottom interface. All enzyme is released in the top phase and no horizontal gas exchange between compartments is assumed. The bubble size d_b is a known, empirical function of the gas flow rate and the installed membrane and will be discussed in Section 2.2.3. It defines the introduced bubble surface flow rate $\dot{A}_b$ under the assumption of spherical bubbles. Thus, the molar flow rate of flotation is defined as

$$\dot{M}_f(i,j,t) = (-1)^i \dot{A}_b(j,t)\Gamma(j,t) = (-1)^i \frac{6\dot{V}_g(j)\Gamma(j,t)}{d_b(j)} \quad . \tag{3}$$

Modeling the molar surface concentration Γ is challenging because enzymes can adsorb in different orientations in multiple layers [25,26]. Furthermore, all processes are non-stationary and may be limited by different transport phenomena in the solution [25,27]. For now, we assume that the adsorption/desorption equilibrium is reached instantaneously and that the molar surface concentration in compartment j ($\Gamma(j,t)$) can be described according to the Langmuir adsorption model

$$\Gamma(j,t) = \frac{M(j,t)}{A_b(j,t)} = \Gamma_{max}\frac{K\,c(1,j,t)}{1 + K\,c(1,j,t)} \quad , \tag{4}$$

where Γ_{max} is the maximum molar surface concentration, K is an equilibrium constant and $c(1,j,t)$ is the current molar concentration in the bottom phase. Both Γ_{max} and K are generally unknown model parameters that have to be adjusted to experiments. Note that Eq. (4) is a strong simplification and will be discussed in detail in Section 3.3.

The mass transfer by extraction through the top/bottom interface is defined by [28]

$$\dot{M}_e(i,j,t) = k_e A_e(j,t)(c_\infty(i,j,t) - c(i,j,t)) \quad , \tag{5}$$

where k_e is the mass transfer coefficient and $A_e(j)$ is the liquid/liquid interfacial area. Due to phase mixing, $A_e(j)$ is an empirical function of the gas flow rate and will be discussed in Section 2.2.4. The equilibrium concentration $c_\infty(i,j,t)$ is calculated for the bottom phase according to

$$c_\infty(1,j,t) = \frac{c(0,j,t) + c(1,j,t)\frac{V(1,j)}{V(0,j)}}{K_p + \frac{V(1,j)}{V(0,j)}} \quad , \tag{6}$$

assuming a constant partition coefficient between top and bottom phase

$$K_p = \frac{c(0,j,t)}{c(1,j,t)} \quad . \tag{7}$$

Inserting Eqs. (2), (3) and (5) into Eq. (1) yields a set of six ODEs for the molar concentration in all compartments $\mathbf{c}(t)$. Given an initial condition $\mathbf{c}(0)$, and a set of boundary conditions, this system is numerically solvable. Table 2 lists all relevant experimental parameters. A provided value indicates that they are constant throughout all simulations, while otherwise their value has to be set, e.g. according to a specific experiment. Initially, all compartments contain their respective feed concentrations, i.e.

$$c(0,j,0) = c_{0,top} \quad | \quad c(1,j,0) = c_{0,bot} \quad . \tag{8}$$

The separation efficiency $E(t)$ describes the proportion of enzyme that is transported from the bottom into the top phase. It is calculated based on the enzyme concentrations at the inlet ($c_{0,top}$, $c_{0,bot}$) and at the outlet ($c(0,2,t)$) according to

$$E(t) = \frac{\dot{Q}_{top}\left[c(0,2,t) - c_{0,top}\right]}{\dot{Q}_{bot}\,c_{0,bot}} \cdot 100\% \quad . \tag{9}$$

2.2.2. A brief note on possible model extensions

The presented model can be extended to describe multi-component systems, such as complex biosuspensions, by applying Eq. (1) to each species and solving the resulting set of ordinary differential equations. This requires the material-specific description of flotation and extraction rates, while possible interactions can be included as well. Since this yields material-specific separation efficiencies, the selectivity of the process can be quantified. In addition, the model equations used for flotation and extraction in Eqs. (3) and (5) respectively can be adjusted to account for system-specific effects. Examples include an increased adsorption due to collector molecules or the separation of solid particles. Note that all extensions result in an increased amount of kinetic parameters that need to be determined either from specific experiments or from calibration with process data.

2.2.3. Bubble size as function of gas volume flow

The bubble diameter is a function of the volumetric gas flow rate and the porous media, as was investigated in our previous study [29]. In this work, the identical twill weave medium was used. The experimental data for the Sauter mean bubble diameter is shown in Fig. 2 together with the continuous fit

$$d_b(j) = C_1\dot{V}_g(j) + C_2\log\dot{V}_g(j) + C_3 \quad . \tag{10}$$

A root mean squared error (RMSE) of RMSE = 47.8 µm was found for the parameters presented in Table 3. Note that the bubble size distribution is not considered in this work. It could be included by performing a 2D fit of the volume-weighted density distribution $q_3(d_b)$ as function of $\dot{V}_g$ and then integrating Eq. (3) over all diameters weighted with the respective density. This increase in the model's complexity was omitted, since the simplified description with the Sauter mean diameter appears sufficient for our purposes and the distribution shape is rather insensitive to $\dot{V}_g$, limiting the influence of the bubble size distribution.

Table 2
Overview of the (default) parameter settings for the ATPF simulations.

Material Parameters			
ρ_{bot}	1192	kg m^{-3}	Density bottom phase
ρ_{top}	1091	kg m^{-3}	Density top phase
η_{bot}	4.48×10^{-3}	Pa s	Viscosity bottom phase
η_{top}	15.72×10^{-3}	Pa s	Viscosity top phase
M_{enz}	14 500	g mol^{-1}	Molar mass enzyme
Process Parameters			
t_{exp}	*variable*	min	Experiment time
$\dot{Q}_{bot}$	*variable*	mL min^{-1}	Volumetric flow rate bottom phase
$\dot{Q}_{top}$	*variable*	mL min^{-1}	Volumetric flow rate top phase
$\dot{V}_g(j)$	*variable*	mL min^{-1}	Gas flow rate compartment j
$w_{0,bot}$	*variable*	% (w/w)	Feed concentration enzyme bottom phase (mass fraction)
$w_{0,top}$	0	% (w/w)	Feed concentration enzyme top phase (mass fraction)
Geometric Parameters			
$V_{bot,total}$	0.5	L	Total volume bottom phase
$V_{top,total}$	0.1	L	Total volume top phase

Table 3
Numerical values of the model coefficients C_1, C_2 and C_3 for estimating $d_b(j)$, $\overline{h}$ and $\overline{v}$ from Eqs. (10) and (15). In all cases, $\dot{V}_g(j)$ is used in mL min^{-1} and the units of the coefficients are accordingly.

y [Unit]	C_1 [*var*]	C_2 [*var*]	C_3 [*var*]
$d_b(j)$ [µm]	-4.88×10^{-2}	1.39×10^{2}	3.83×10^{2}
$\overline{h}$ [mm]	0.202	0.329	0.475
$\overline{v}$ [–]	1.61×10^{-3}	4.56×10^{-3}	5.27×10^{-3}

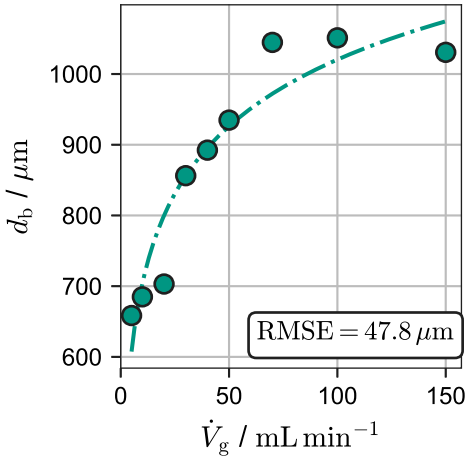

Fig. 2. Sauter mean bubble diameter over gas flow rate for twill weave. Experimental data from [29] and continuous fit.

2.2.4. Effective liquid/liquid interface

Eq. (5) calculates the molar flow rate across the liquid/liquid interface based on the interfacial area $A_e(j,t)$. The geometrical dimensions of the flotation basin directly define the interfacial area for the static system $A_{0,e}$. However, the gas bubbles agitate the interface which results in a mixed zone instead of a perfect film (see photos in Section A of the SI). Therein, both phases are dispersed as emulsion, which results in an increased interfacial area available for mass transport. The top phase is assumed to be dispersed in the bottom phase as spherical droplets of fixed diameter d_d with a volume fraction of υ. Thus, the effective interfacial area is linked to the droplet diameter and the height of the mixing zone h as follows:

$$V_{top} = N\frac{\pi d_d^3}{6} = \upsilon V_{bot} \tag{11}$$

$$V = V_{top} + V_{bot} = N\frac{\pi d_d^3}{6}\left(1+\upsilon^{-1}\right) = A_{0,e}h \tag{12}$$

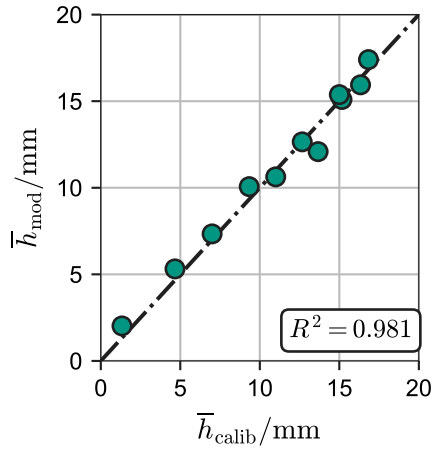

Fig. 3. Parity plot for MLR model on average height of mixing zone.

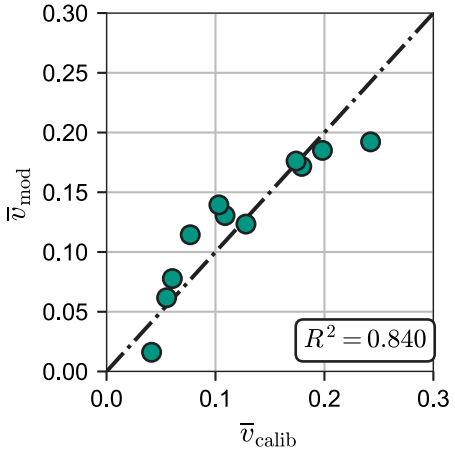

Fig. 4. Parity plot for MLR model on average height of mixing zone.

$$A_e = A_{0,e} + N\pi d_d^2 = A_{0,e}\left(1 + \frac{6h}{d_d\left(1+\upsilon^{-1}\right)}\right) \tag{13}$$

In each compartment, probes are placed right below the interface to measure the conductivity κ (see Fig. 1(a)). It is a measure for the dispersed volume fraction and prior calibration experiments yielded the linear correlation

$$\upsilon = -0.0146 \text{ cm mS}^{-1}\kappa + 0.767 \tag{14}$$

The height of the mixing zone h and the conductivity, i.e. volume fraction υ, strongly depend on the gas volume flow. Calibration experiments with a systematic variation of $\dot{V}_g(j)$ in all compartments were performed and the conductivity as well as height of the mixing zone measured in each compartment. Since neighboring compartments strongly affect each other [21], they cannot be handled individually. Hence, two multiple linear regression models

$$y = C_1\dot{V}_g(0) + C_2\dot{V}_g(1) + C_3\dot{V}_g(2) \tag{15}$$

with $\dot{V}_g(0)$, $\dot{V}_g(1)$ and $\dot{V}_g(2)$ as inputs were trained to predict the average values of either $\overline{h}$ or $\overline{\upsilon}$. The `LinearRegression` class from the Python library `scikit-learn` [30] was used. The resulting coefficients are given in Table 3 and the parity plots are shown in Figs. 3 and 4. $\overline{h}$ is predicted accurately ($R^2 = 0.981$), while predicting $\overline{\upsilon}$ is more uncertain yet satisfactory ($R^2 = 0.840$). Both correlations were implemented in the model leaving d_d to be the only unknown parameter in Eq. (13) that has to be adjusted based on experimental data. A closer look at the data shows that the coefficients for both the $\overline{h}$ and $\overline{\upsilon}$ models increase from compartment 1 to 3. Compartment 3 therefore has a more dramatic effect on the mixing zone. However, the phase mixing in compartment 3 should be kept relatively low to allow phase separation before the phases leave the flotation tank. Note that during processing, i.e. application of the model, κ is measured online and can therefore be used directly e.g. in the scenario of model predictive control. The obtained correlation for $\overline{\upsilon}$ is therefore only necessary in cases where the model is used in isolation.

2.3. Numerical optimization

All unknown model parameters are denoted as $\mathcal{M}$ and are assumed to be system-specific, meaning that they do not depend on process parameters and are therefore constant for all experiments. Data of the enzyme concentration of the outflow of the top phase with respect to time ($c(0, 2, t)$) is available for each experiment. This data is denoted as $C_{exp} \in \mathbb{R}^{N\times T}$, where N is the number of experiments and T is the number of discrete time steps. In total $N = 48$ experiments with varying process parameters were used in this study. All experiments are listed in Table C.1 in the SI. For any given set of model parameters $\mathcal{M}$, the full experimental design can be simulated under consideration of the employed process parameters. The modeled enzyme concentrations C_{mod} are also of dimension $\mathbb{R}^{N\times T}$, as long as the numerical solution is stored at the same time steps as the experiment. The optimal set of model parameters $\mathcal{M}_{opt}$ is obtained by solving the following optimization problem based on the root mean squared error (RMSE):

$$\min_{\mathcal{M}} \sqrt{\frac{1}{NT}\sum \left[C_{exp} - C_{mod}(\mathcal{M})\right]^2} \tag{16}$$

Optimization is performed with the global optimization algorithm differential evolution based on Storn and Price [31] and implemented in `differential_evolution()` from the `scipy.optimize` module [32]. Initial sampling was based on the latin hypercube method [33] to ensure broad coverage of the search space. Found optima are polished with a local optimizer based on Byrd et al. [34] and implemented in `minimize()`. The search space (bounds) for the respective parameters and functional arguments to the optimizers are provided in Table B.1 in the SI.

3. Results & discussion

3.1. Sensitivity analysis and model reduction

The ATPF model described in Section 2.2 contains three model parameters that require adjustment to experimental data: The maximum molar surface concentration Γ_{max}, the Langmuir equilibrium constant K and the diameter of dispersed top phase droplets in the mixing zone d_d. Each unknown parameter makes the numerical optimization from Section 2.3 harder and slower. Therefore a variance-based sensitivity analysis was performed to quantify the relative importance of all three model parameters with the `SALib` package [35] used together with Saltelli's sampling method. $N = 8192$ samples with systematic variations of all three model parameters within specified bounds were created and the cost function in Eq. (16) evaluated. It is crucial to define realistic bounds for all parameters, which are listed in Table 4. The lower bound for Γ_{max} is set at 10^{-7} mol m^{-2}, which corresponds to typical values of single layer adsorption for similar enzymes [25]. The upper bound is set at 10^{-4} mol m^{-2} to allow for possible multilayer adsorption. K was varied between 1 m^3 mol^{-1} and 100 m^3 mol^{-1}, which covers the reported range of values for similar enzymes [25]. For d_d, no literature values are available, however, due to the moderate energy input by the bubbles, the macroemulsion regime is assumed, which places the bounds at 1 μm and 100 μm respectively [36,37]. The total Sobol indices S_T describe the total contribution of a parameter to the output variance of a function, accounting for both its direct effect and all interaction effects with other parameters. It therefore measures the total influence that each parameter has on the cost function and the model in general.

Table 4
Bounds and results of the Sobol sensitivity analysis.

Parameter	Unit	Bounds	S_T
Γ_{max}	mol m^{-2}	$(10^{-7}, 10^{-4})$	0.076
K	m^3 mol^{-1}	$(1, 100)$	0.021
d_d	m	$(10^{-5}, 10^{-4})$	0.968

The resulting values are given in Table 4. It is apparent that the model is highly sensitive towards variations of d_d, which explain roughly 97% of the total variance, while both flotation parameters show significantly lower values. This indicates that extraction is more relevant for describing the observed experimental effects, a discussion that will be elaborated in the following sections. Furthermore, the total Sobol index of K is lower than the one of Γ_{max}. This means that the adsorption is relatively independent of the enzyme concentration and that a constant surface density Γ_{max} is sufficient to model the mass transport by flotation. Due to the relatively low impact of flotation in general, the usage of two parameters seems not justifiable and K is therefore set constant at 12.5 m^3 mol^{-1} for all following simulations. This corresponds to the value of lysozyme [25], an enzyme with similar molar mass. With this, the model is reduced to two unknown parameters $\mathcal{M} = \{\Gamma_{max}, d_d\}$, which makes it less prone to overfitting and helps to make the numerical optimization procedure more reliable.

3.2. Model calibration and accuracy

The reduced ATPF model contains two unknown parameters that have to be adjusted to experimental data. To investigate which transport mechanism is dominant, three separate case studies were performed:

(I) Full ATPF model with extraction and flotation
(II) Only mass transport via extraction ($\dot{M}_f = 0$)
(III) Only mass transport via flotation ($\dot{M}_e = 0$)

For each case, the model parameters were optimized according to the procedure detailed in Section 2.3. Table 5 provides the resulting values of the model parameters, while Table B.1 in the SI lists all optimization parameters. Most notably, the search space was set to the previously discussed bounds from Section 3.1.

Fig. 5 shows the parity plot for all 48 experiments for case (I), distinguished by marker and color. Two edge cases (a) and (b) are highlighted by squared marker, no transparency and two arrows that will be discussed in Section 3.4. Overall, the experimental data are well represented by the model. This is supported by an RMSE value of 6.20×10^{-3}, meaning that w_{mod} and w_{exp} deviate on average by

Table 5
Optimized model parameters $\mathcal{M}_{opt}$ for the respective simulation cases.

Parameter	Unit	Case (I)	Case (II)	Case (III)
Γ_{max}	mol m^{-2}	9.27×10^{-6}	–	1×10^{-4}
d_d	m	4.47×10^{-5}	3.85×10^{-5}	–
RMSE (Eq. (16))	–	6.20×10^{-3}	6.32×10^{-3}	1.52×10^{-2}

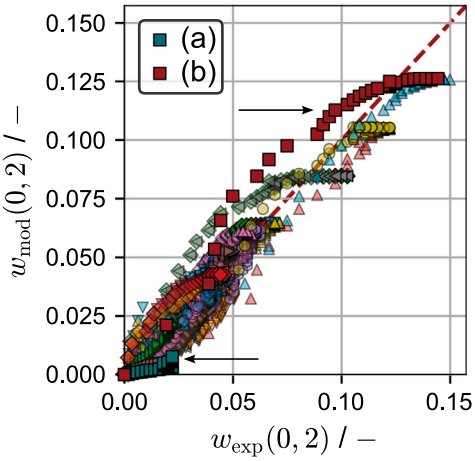

Fig. 5. Parity plot for all 48 experiments for simulation case (I).

roughly 0.62% (w/w) across all points in time of all experiments. It should be noted that these experiments include variations of the gas flow rate combination, feed rates and feed concentrations, as detailed in Table C.1 in the SI. Obtaining a mechanistic model this accurate, which only relies on two empirical parameters with physical relevance therefore highlights the suitability of the made assumptions. It is also noteworthy that the UV/vis analysis, i.e. the experimental data, only has a resolution of ±0.17% (w/w), further underlining the accuracy of the model.

By splitting the contributions of $\dot{M}_f$ in Eq. (3) and $\dot{M}_e$ in Eq. (5), it is possible to integrate both contributions individually while solving the system of ODEs. This allows for quantifying the relative contribution of mass transfer by extraction

$$X_{e,int} = \int_0^{t_{exp}} \frac{\dot{M}_e}{(\dot{M}_e + \dot{M}_f)} dt \tag{17}$$

towards the overall enzyme mass transport through the interface. The results are visualized in Fig. 6 over the integral gas volume flow rate $\sum \dot{V}_g$ together with a simple linear regression line. Additionally, the average RMSE for each experiment is shown on the secondary axis. With increasing integral gas volume flow, the relevance of extraction increases and the RMSE decreases. From an integral gassing of 20 mL min^{-1} onward, the relative contribution of extraction is around 80%. This means that the mass transfer in case (I) is mainly caused by extraction, while the bubbles facilitate phase mixing as described in Section 2.2.4. The decreasing trend in RMSE shows that ATPF experiments with low integral gas flow rates are less well represented by the model. This will be discussed separately in Section 3.4.

The dominance of extraction is further supported by simulation cases (II) and (III): In case (II) mass transfer by flotation is set to zero. This is compensated by a slightly smaller value of d_d, resulting in higher interfacial area and higher transport by extraction. However, both the value of d_d and of the RMSE are very similar to case (I). Therefore, the physical processes are well explained by the pure extraction and raise doubts on the significance of the transport via flotation. In case (III), the loss of the extraction transport is compensated by an increase in Γ_{max} by a factor of 10. However, flotation alone is not able to represent the experimental data well, as shown in a more than doubled RSME value.

3.3. Discussion on model assumptions and numeric values of the optimized model parameters

The presented model is subject to simplifying assumptions. Considering extraction, we assumed a perfectly monodisperse emulsion droplet size distribution with an optimized droplet size of roughly 35–45 µm. This size range seems plausible as the droplets in the mixing zone are not visible with the naked eye (see photos in Section A of SI). Furthermore, this value falls perfectly in the typical range of macroemulsions with moderate energy input [36,37]. Additionally, we assumed that each phase is perfectly mixed, i.e. that the enzyme concentrations in the extraction zone correspond to the bulk concentrations in the top and bottom phase. In reality, concentration gradients are lower, since the replacement of both phases in the extraction zone requires time and both bulk phases themselves are imperfectly mixed. Nevertheless, we expect this to play a subordinate role because the system is strongly agitated by the bubbles, which increases phase exchange in the extraction zone and because the droplet diameter could be smaller to counteract this effect and still be physically plausible.

Considering flotation, we assumed a surface loading according to the Langmuir adsorption model in Eq. (4). Although we do not strictly assume single layer adsorption by keeping the parameter Γ_{max} variable, the Langmuir model still assumes saturation of the gas/liquid interface. The obtained value of $\Gamma_{max} \approx 10^{-5}$ mol m^{-2} in case (I) seems unrealistically high when considering all available data in literature: Although no data on phospholipase A_2 was found specifically, we can assume that it behaves similar to lysozyme due to its similar molecular weight [38]. Monolayer adsorption for lysozyme allows for a surface concentration of roughly 2×10^{-7} mol m^{-2} [25,39]. However, the surface is already saturated at bulk concentrations of $w \approx 10^{-3}$ % (w/w). At higher concentrations, multilayer adsorption occurs and the surface concentration rapidly increases proportional to the bulk concentration [25]. Experimental data is only available until $w = 10^{-2}$ % (w/w), where the surface loading reaches approximately 10^{-6} mol m^{-2}, thus it seems plausible for the loading to further increase by a factor of 10 for the bulk concentrations considered here. However, all presented data is for the equilibrium at stationary interfaces. During ATPF, bubbles rise through the bottom phase and are subjected to shear stress. This leads to a change in the adsorption rate of the enzymes and their distribution at the gas/liquid interface [40,41]. Enzymes in subsequent adsorption layers are "loosely" bound [25] and are easily removed from the interface. This is similar to ions adsorbing in the diffusive layer around charged particles in solution: When agitated, the diffusive layer is sheared off, while the strongly adsorbed Stern layer remains, the effect that is exploited to measure the zeta potential [42,43]. Hence, it remains doubtful if a surface loading 100-times larger than monolayer adsorption can be supported by the moving bubble surface.

Furthermore, the Langmuir model only describes the steady state between adsorption and desorption, hence the model assumes that this equilibrium is instantaneously reached. In reality, the surface concentration is a function of time $\Gamma = f(t)$. The molecules must first diffuse from the bulk solution into the interfacial sublayer to become irreversibly adsorbed at the air/liquid interface. They then unfold at the interface [40]. A prominent Equation in literature, to describe this time dependence is given by [25,44,45]

$$\Gamma(t) = 2c \left(\frac{D\,t}{\pi} \right)^{0.5} , \tag{18}$$

where c is the molar bulk enzyme concentration and D the diffusion coefficient. This equation is derived by modeling the transport as an infinite-medium diffusion problem [25] where enzyme is instantaneously and irreversibly adsorbed by the interface, i.e. where the bulk concentration just below the surface is assumed to be 0. The rising velocity of the air bubbles can be estimated by Stokes' law [46]. By assuming a bubble diameter of 856.24 µm, a rising time of the bubble through the bottom phase in the order of 1 s is calculated for a bottom

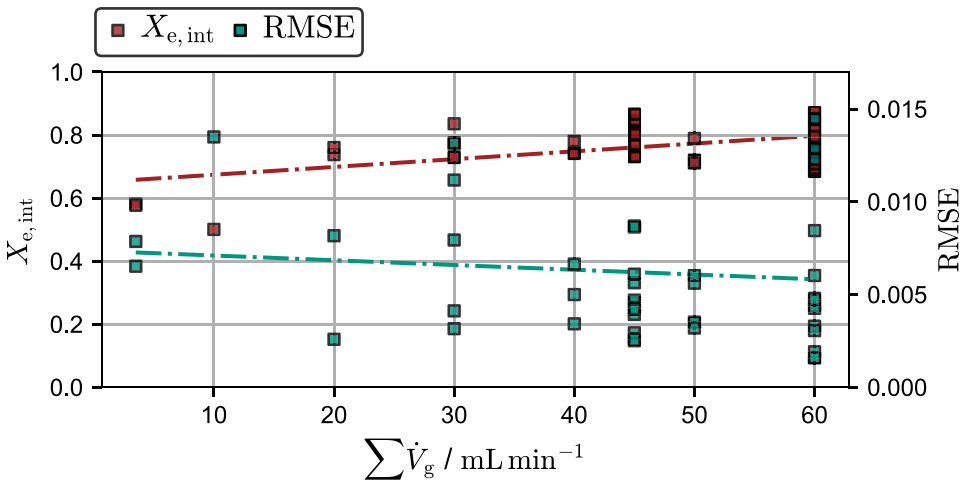

Fig. 6. Relative importance of mass transport through extraction, and RMSE over integral gas volume flow.

Table 6
Γ_{1s} of different enzymes at an air/water interface.

	Unit	Lysozyme	β-casein	BT-HAase
M	kDa	14.5	24	65
c	mol m^{-3}	5.2×10^{-5}	3.0×10^{-5}	3.0×10^{-4}
D	m^2 s^{-1}	8×10^{-10}	5×10^{-10}	6×10^{-10}
Γ_{1s}	mol m^{-2}	1.7×10^{-9}	7.7×10^{-10}	8.5×10^{-9}
Γ_{mono}	mol m^{-2}	2.0×10^{-7}	1.1×10^{-7}	–
Ref.		[25,47]	[25,47]	[45]

phase height of 9.7 cm. The assumed diameter corresponds to a gas volume flow of 30 ml min^{-1} using a twill weave as the porous medium (see Fig. 2). As no gas volume flows greater than 30 ml min^{-1} are used in this work, this can be considered a minimum estimate for the available adsorption time.

Table 6 summarizes the expected molar surface concentrations Γ_{1s} after 1 s calculated from Eq. (18) for three different enzymes based on literature data together with the maximum loading of a monolayer (if available). It is apparent that 1 s is not sufficient to saturate the monolayer at these bulk concentrations. This is also supported by experiments of the adsorption kinetic, where steady state is only reached after hours of the experiment [25,27]. In this work, enzyme concentrations are in the order of 1 mol m^{-3} and hence adsorption is expected to be much faster according to Eq. (18). Nevertheless, the linear dependence on c in Eq. (18) is not expected to hold for arbitrary high concentrations since at some point transport processes inside the bulk phase will become limiting and the assumptions for deriving Eq. (18) are not justified anymore.

In summary, this discussion shows that while the mass transport via extraction is plausible, the obtained values for mass transport via flotation are highly questionable: For one, the interface is not expected to have the maximum capacity for the required amount of enzyme and additionally, enzyme adsorption cannot be expected to occur within seconds. Specific experiments are required to quantify the adsorption kinetics of enzymes on the surface of a rising bubble. Particle image velocimetry (PIV) combined with particle tracking velocimetry (PTV) is a suitable technique for this purpose. It allows to visualize the flow acting on the bubble and to measure the adsorption of tracer molecules with high temporal and spatial resolution [40]. With the additional use of profile analysis tensiometry (PAT), it is possible to determine the change in surface properties of the adsorbed substance [40,48]. This includes the surface tension as well as the concentration and distribution of the adsorbed molecules on the bubble surface [40]. Such measurements are beyond the scope of this work, but are important for future research.

3.4. Discussion of selected edge cases

This section discusses the two edge cases highlighted in Fig. 5 in more detail. Fig. 6 indicated that the model is less accurate when predicting experiments at very low gas flow rates, e.g. 10-00-00, for which an exemplary result is shown in Fig. 7(a). The model predicts a significantly slower increasing and overall lower enzyme concentration than measured in the ATPF experiment. Considering the previously discussed dominance of extraction, this is likely due to a poor representation of the phase mixing conditions by the correlations from Section 2.2.4. Phase mixing is underestimated for lower gas flow rates, which can be explained by the used multiple linear regression model. It is reasonable to assume that the relationship between gas flow rate and phase mixing is non-linear and especially during creation of the mixing zone, i.e. at lower gas flow rates, more pronounced. More data in this lower parameter regime would be necessary to train non-linear regression models that are capable of adequately representing this effect. However, these very low gas flow rates were mostly tested for academic purposes and not really relevant to regular processing conditions, as higher concentrations are desirable, which in turn are achieved with higher integral gas flows.

On the other end, an experiment with high gas flow rates, i.e. 30–20–10 and high enzyme concentrations (3% (w/w)) was highlighted in Fig. 5, which appears to be represented quite well by the model. However, all experiments that reach high enzyme concentrations seem to level off in the parity plot meaning that the model underestimates enzyme concentrations at later process times. The detailed results are shown in Fig. 7(b). The concentration profile is well predicted by the model up to a time of $t = 20$ min. However, after $t = 25$ min, the experimental concentration continues to increase steadily. The reason for this difference is more likely to be found in the experimental data, since a steady state, as predicted by the model, is to be expected. The viscosity of the top phase increases significantly at high enzyme concentrations, which resulted in clogging of the UV/vis flow cell with loaded top phase during certain experiments. Although these experiments were discarded and not considered in this study, it is plausible that an accumulation of enzyme may still occur in the flow cell without complete clogging. This would explain the continuously rising enzyme concentration and deviations to the model.

4. Conclusion

This study developed a physical process model for aqueous two-phase flotation (ATPF). The model was able to accurately represent experiments with broad variations in gas flow rate combinations, feed rates and feed concentrations. This is noteworthy because it is purely

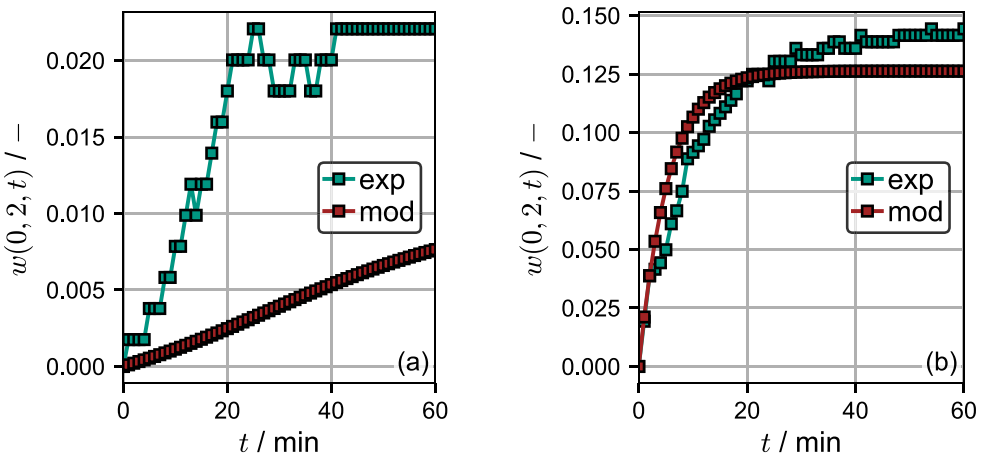

Fig. 7. Exemplary results for two edge cases highlighted in Fig. 5. (a) Gas flow rate combination, 10-00-00 (mL min^{-1}) and feed concentration of 1% (w/w), (b) gas flow rate combination of 30-20-10 (mL min^{-1}) and a feed concentration of 3% (w/w).

mechanistic, except for experimentally determined correlations and two empirical parameters Γ_{max} and d_d. The optimization to experiments yielded plausible values for these parameters and hence, we concluded that the assumptions made were justified.

This model is highly valuable for future process developments: First, it enables the development of a model predictive control (MPC) strategy. Due to the accuracy of the model, a reliable, autonomous and continuous ATPF process can be envisioned. Second, the model offers insights into non-measurable phenomena on the micro scale and increases our understanding of ATPF in general. Both mass transport mechanisms flotation and extraction are responsible for the vertical mass transfer of biomolecules from the bottom to the top phase. Until now, flotation has been assumed to be the dominant transport mechanism. Model development and comparison with experimental data strongly support the opposite, namely that extraction is the dominant mechanism and accounts for at least 80% of the integral mass transfer. There are several reasons for this: First, a sensitivity analysis revealed that the model is rather insensitive to flotation-specific parameters and that flotation is not able to explain the experimentally observed variance. Second, it was found that a model that only considers transport via extraction achieves a very similar accuracy to the model that includes both. On the other hand, including only flotation resulted in significantly worse predictions. Finally, and most convincingly, the required surface loading of the bubbles to explain the observed mass transport was found to be implausible as the surface capacity is expected to be lower and the time available for enzymes to attach to the surface is not expected to be sufficient. It should be noted that gas input is still important since it facilitates strong phase mixing, which significantly increases the interfacial area for mass transport by extraction.

With these new findings, the ATPF setup can be further optimized to enhance phase mixing and extraction. Computational Fluid Dynamics (CFD) simulations can be used to further refine the model and better describe the mixing zone. This will also allow for optimization of the flotation tank geometry. Future experimental studies should determine the adsorption kinetics of enzymes on the surface of rising bubbles to validate the model parameter Γ_{max} found in this work, refine the used flotation model and clarify the relevance of flotation in general. In addition, the presented process model is universally applicable to a wide range of material systems and can even be extended to multi-material systems. This enables the prediction of selective separation in enzyme mixtures or complex biosuspensions such as industrial fermentation broths. However, the calibration of the material-specific flotation and extraction parameters requires experimental data, which should be the focus of future studies. Nevertheless, the presented model lays the foundation for model-based optimization of selective separation in complex suspensions via ATPF.

CRediT authorship contribution statement

Kim Carina Lohfink: Conceptualization, Data curation, Formal analysis, Investigation, Methodology, Validation, Visualization, Writing – original draft. **Hermann Nirschl:** Funding acquisition,Project administration,Resources, Supervision,Writing – review & editing. **Frank Rhein:** Conceptualization, Data curation,Formal analysis, Investigation, Methodology, Resources, Supervision, Validation, Visualization, Writing – original draft.

Declaration of competing interest

The authors declare that they have no known competing financial interests or personal relationships that could have appeared to influence the work reported in this paper.

Acknowledgment

This research was funded by the German Research Foundation within the priority program SPP 2364 “Autonomous Processes in Particle Technology” (Grant number: 504452366).

Appendix A. Supplementary data

Supplementary material related to this article can be found online at https://doi.org/10.1016/j.seppur.2025.133100.

Data availability

All data used in this study is available at KITopen/Radar [49]. All Python scrips and the ATPF model class are publicly available in the Github repository pdhs-group/ATPF.

References

[1] P. Binod, P. Palkhiwala, R. Gaikaiwari, K.M. Nampoothiri, A. Duggal, K. Dey, A. Pandey, Industrial Enzymes - Present status and future perspectives for India, JSIR 72 (05) (2013).

[2] V. Yadav, S. Biswas, A. Goyal, Enzymes of industrial significance and their applications, in: P. Verma (Ed.), Industrial Microbiology and Biotechnology: An Insight Into Current Trends, Springer Nature, Singapore, 2024, pp. 277–307, http://dx.doi.org/10.1007/978-981-97-1912-9_11.

[3] A. Antecka, M. Blatkiewicz, T. Boruta, A. Górak, S.a. Ledakowicz, Comparison of downstream processing methods in purification of highly active laccase, Bioprocess Biosyst. Eng. 42 (10) (2019) 1635–1645, http://dx.doi.org/10.1007/s00449-019-02160-3.

[4] S.Y. Lee, I. Khoiroh, T.C. Ling, P.L. Show, Aqueous two-phase flotation for the recovery of biomolecules, Sep. Purif. Rev. 45 (1) (2016) 81–92, http://dx.doi.org/10.1080/15422119.2015.1007147.

[5] P.-y. Bi, D.-q. Li, H.-r. Dong, A novel technique for the separation and concentration of penicillin G from fermentation broth: Aqueous two-phase flotation, Sep. Purif. Technol. 69 (2) (2009) 205–209, http://dx.doi.org/10.1016/j.seppur.2009.07.019.

[6] R. Hatti-Kaul, Aqueous two-phase systems, Mol. Biotechnol. 19 (2001).

[7] P.L. Show, C.P. Tan, M.S. Anuar, A. Ariff, Y.A. Yusof, S.K. Chen, T.C. Ling, Direct recovery of lipase derived from Burkholderia cepacia in recycling aqueous two-phase flotation, Sep. Purif. Technol. 80 (3) (2011) 577–584, http://dx.doi.org/10.1016/j.seppur.2011.06.013.

[8] M.A. Torres-Acosta, K. Mayolo-Deloisa, J. González-Valdez, M. Rito-Palomares, Aqueous two-phase systems at large scale: Challenges and opportunities, Biotechnol. J. 14 (1) (2019) 1800117, http://dx.doi.org/10.1002/biot.201800117, _eprint: https://onlinelibrary.wiley.com/doi/pdf/10.1002/biot.201800117.

[9] P.-y. Bi, L. Chang, Y.-l. Mu, J.-y. Liu, Y. Wu, X. Geng, Y. Wei, Separation and concentration of baicalin from Scutellaria Baicalensis Georgi extract by aqueous two-phase flotation, Sep. Purif. Technol. 116 (2013) 454–457, http://dx.doi.org/10.1016/j.seppur.2013.06.024.

[10] P.L. Show, C.W. Ooi, M.S. Anuar, A. Ariff, Y.A. Yusof, S.K. Chen, M.S.M. Annuar, T.C. Ling, Recovery of lipase derived from Burkholderia cenocepacia ST8 using sustainable aqueous two-phase flotation composed of recycling hydrophilic organic solvent and inorganic salt, Sep. Purif. Technol. 110 (2013) 112–118, http://dx.doi.org/10.1016/j.seppur.2013.03.018.

[11] M. Li, H.-r. Dong, The investigation on the aqueous two-phase floatation of lincomycin, Sep. Purif. Technol. 73 (2) (2010) 208–212, http://dx.doi.org/10.1016/j.seppur.2010.04.002.

[12] S.V. Pakhale, M.D. Vetal, V.K. Rathod, Separation of Bromelain by Aqueous two phase flotation, Sep. Sci. Technol. 48 (6) (2013) 984–989, http://dx.doi.org/10.1080/01496395.2012.712596.

[13] L. Chang, Q. Shao, X. Xi, Q. Chu, Y. Wei, Separation of four flavonol glycosides from Solanum rostratum Dunal using aqueous two-phase flotation followed by preparative high-performance liquid chromatography, J. Sep. Sci. 40 (3) (2017) 804–812, http://dx.doi.org/10.1002/jssc.201600922, _eprint: https://onlinelibrary.wiley.com/doi/pdf/10.1002/jssc.201600922.

[14] N.L. Md Sidek, J.S. Tan, S. Abbasiliasi, F.W.F. Wong, S. Mustafa, A.B. Ariff, Aqueous two-phase flotation for primary recovery of bacteriocin-like inhibitory substance (BLIS) from Pediococcus acidilactici Kp10, J. Chromatogr. B 1027 (2016) 81–87, http://dx.doi.org/10.1016/j.jchromb.2016.05.024.

[15] J. Han, Y. Wang, C. Yu, C. Li, Y. Yan, Y. Liu, L. Wang, Separation, concentration and determination of chloramphenicol in environment and food using an ionic liquid/salt aqueous two-phase flotation system coupled with high-performance liquid chromatography, Anal. Chim. Acta 685 (2) (2011) 138–145, http://dx.doi.org/10.1016/j.aca.2010.11.033.

[16] C.E. de Araújo Padilha, P.V.F. Dantas, C.d.C. Nogueira, A.L.d.S. Leitão, H.N. Almeida, D.F. de Santana Souza, J.A.d. Oliveira, G.R. de Macedo, E.S. dos Santos, Enhancing the recovery and concentration of polyphenols from camu-camu (Myrciaria dubia h.b.k. McVaugh) by aqueous two-phase flotation and scale-up process, Sep. Sci. Technol. 53 (13) (2018) 2126–2135, http://dx.doi.org/10.1080/01496395.2018.1442865.

[17] Y. Wang, X.-h. Xu, J. Han, Y.-s. Yan, Separation/enrichment of trace tetracycline antibiotics in water by [Bmim]BF4–(NH4)2SO4 aqueous two-phase solvent sublation, Desalination 266 (1) (2011) 114–118, http://dx.doi.org/10.1016/j.desal.2010.08.010.

[18] J. Zhuang, W. Yang, X. Chen, F. Jiao, Enantioseparation of phenylsuccinic acid enantiomers using aqueous two-phase flotation and their determination by HPLC and UV detection, Chromatographia 77 (9) (2014) 679–685, http://dx.doi.org/10.1007/s10337-014-2668-y.

[19] L. Jakob, M. Heinzmann, H. Nirschl, Development of a continuous aqueous two-phase flotation process for the downstream processing of biotechnological products, Sep. Purif. Technol. 278 (2021) 119657, http://dx.doi.org/10.1016/j.seppur.2021.119657.

[20] L. Jakob, H.K. Baust, L. Griesinger, H. Nirschl, Optimized apparatus design for continuous aqueous two-phase flotation (ATPF), Separations 10 (9) (2023) 511, http://dx.doi.org/10.3390/separations10090511.

[21] K.C. Lohfink, K. Baumgärtner, M. Kirsch, F. Rhein, M. Diehl, H. Nirschl, Online monitoring of continuous aqueous two-phase flotation (ATPF) for the development of an autonomous control strategy, Chem. Eng. Sci. 297 (2024) 120287, http://dx.doi.org/10.1016/j.ces.2024.120287.

[22] T. Gamer, M. Hoernicke, B. Kloepper, R. Bauer, A.J. Isaksson, The autonomous industrial plant – future of process engineering, operations and maintenance, J. Process Control 88 (2020) 101–110, http://dx.doi.org/10.1016/j.jprocont.2020.01.012.

[23] H. Edelhoch, Spectroscopic determination of Tryptophan and Tyrosine in proteins*, Biochemistry 6 (7) (1967) 1948–1954, http://dx.doi.org/10.1021/bi00859a010.

[24] F.S. Rocha, A.J. Gomes, C.N. Lunardi, S. Kaliaguine, G.S. Patience, Experimental methods in chemical engineering: Ultraviolet visible spectroscopy—UV-Vis, Can. J. Chem. Eng. 96 (12) (2018) 2512–2517, http://dx.doi.org/10.1002/cjce.23344, _eprint: https://onlinelibrary.wiley.com/doi/pdf/10.1002/cjce.23344.

[25] R.Z. Guzman, R.G. Carbonell, P.K. Kilpatrick, The adsorption of proteins to gas-liquid interfaces, J. Colloid Interface Sci. 114 (2) (1986) 536–547, http://dx.doi.org/10.1016/0021-9797(86)90439-X.

[26] L.K. James, L.G. Augenstein, Adsorption of enzymes at interfaces: Film formation and the effect on activity, in: Advances in Enzymology and Related Areas of Molecular Biology, 1966, pp. 1–40, http://dx.doi.org/10.1002/9780470122730.ch1.

[27] D.E. Graham, M.C. Phillips, Proteins at liquid interfaces: I. Kinetics of adsorption and surface denaturation, J. Colloid Interface Sci. 70 (3) (1979) 403–414, http://dx.doi.org/10.1016/0021-9797(79)90048-1.

[28] I. Kaplanow, F. Goerzgen, J. Merz, G. Schembecker, Mass transfer of proteins in aqueous two-phase systems, Sci. Rep. 9 (1) (2019) 3692, http://dx.doi.org/10.1038/s41598-019-39797-9.

[29] L. Jakob, J. Singer, H. Nirschl, Importance of gas input in aqueous two-phase flotation (ATPF), Chem. Eng. Sci. 233 (2021) 116391, http://dx.doi.org/10.1016/j.ces.2020.116391.

[30] F. Pedregosa, G. Varoquaux, A. Gramfort, V. Michel, B. Thirion, O. Grisel, M. Blondel, P. Prettenhofer, R. Weiss, V. Dubourg, J. Vanderplas, A. Passos, D. Cournapeau, M. Brucher, M. Perrot, E. Duchesnay, Scikit-learn: Machine learning in Python, J. Mach. Learn. Res. 12 (2011) 2825–2830.

[31] R. Storn, K. Price, Differential evolution – A simple and efficient heuristic for global optimization over continuous spaces, J. Global Optim. 11 (4) (1997) 341–359, http://dx.doi.org/10.1023/A:1008202821328.

[32] P. Virtanen, R. Gommers, T.E. Oliphant, M. Haberland, T. Reddy, D. Cournapeau, E. Burovski, P. Peterson, W. Weckesser, J. Bright, S.J. van der Walt, M. Brett, J. Wilson, K.J. Millman, N. Mayorov, A.R.J. Nelson, E. Jones, R. Kern, E. Larson, C.J. Carey, İ. Polat, Y. Feng, E.W. Moore, J. VanderPlas, D. Laxalde, J. Perktold, R. Cimrman, I. Henriksen, E.A. Quintero, C.R. Harris, A.M. Archibald, A.H. Ribeiro, F. Pedregosa, P. van Mulbregt, SciPy 1.0 Contributors, SciPy 1.0: Fundamental algorithms for scientific computing in python, Nature Methods 17 (2020) 261–272, http://dx.doi.org/10.1038/s41592-019-0686-2.

[33] M.D. McKay, R.J. Beckman, W.J. Conover, A comparison of three methods for selecting values of input variables in the analysis of output from a computer code, Technometrics 21 (2) (1979) 239–245, http://dx.doi.org/10.2307/1268522.

[34] R.H. Byrd, P. Lu, J. Nocedal, C. Zhu, A limited memory algorithm for bound constrained optimization, SIAM J. Sci. Comput. 16 (5) (1995) 1190–1208, http://dx.doi.org/10.1137/0916069.

[35] J. Herman, W. Usher, SALib: An open-source Python library for sensitivity analysis, J. Open Source Softw. 2 (9) (2017) http://dx.doi.org/10.21105/joss.00097.

[36] M. L'Estimé, M. Schindler, N. Shahidzadeh, D. Bonn, Droplet size distribution in emulsions, Langmuir 40 (1) (2024) 275–281, http://dx.doi.org/10.1021/acs.langmuir.3c02463.

[37] H. Karbstein, H. Schubert, Developments in the continuous mechanical production of oil-in-water macro-emulsions, Chem. Eng. Process.: Process. Intensif. 34 (3) (1995) 205–211, http://dx.doi.org/10.1016/0255-2701(94)04005-2.

[38] I. Kudo, M. Murakami, Phospholipase A2 enzymes, Prostaglandins Other Lipid Mediat. 68–69 (2002) 3–58, http://dx.doi.org/10.1016/S0090-6980(02)00020-5.

[39] D.E. Graham, M.C. Phillips, Proteins at liquid interfaces: II. Adsorption isotherms, J. Colloid Interface Sci. 70 (3) (1979) 415–426, http://dx.doi.org/10.1016/0021-9797(79)90049-3.

[40] M. Eftekhari, K. Schwarzenberger, S. Heitkam, K. Eckert, Interfacial flow of a surfactant-laden interface under asymmetric shear flow, J. Colloid Interface Sci. 599 (2021) 837–848, http://dx.doi.org/10.1016/j.jcis.2021.04.126.

[41] M. Eftekhari, K. Schwarzenberger, S. Heitkam, A. Javadi, A. Bashkatov, S. Ata, K. Eckert, Interfacial behavior of particle-laden bubbles under asymmetric shear flow, Langmuir 37 (45) (2021) 13244–13254, http://dx.doi.org/10.1021/acs.langmuir.1c01814.

[42] J.N. Israelachvili, Intermolecular and Surface Forces, 3. ed., Elsevier, Amsterdam, Heidelberg [u.a.], 2011.

[43] M. Elimelech, Particle Deposition and Aggregation : Measurement, Modelling and Simulation, 1. publ., in: Colloid and surface engineering series, Butterworth-Heinemann, Woburn, Mass., 1998.

[44] G. Yampolskaya, D. Platikanov, Proteins at fluid interfaces: Adsorption layers and thin liquid films, Adv. Colloid Interface Sci. 128–130 (2006) 159–183, http://dx.doi.org/10.1016/j.cis.2006.11.018.

[45] D.S. Monteiro, T.M. Nobre, M.E.D. Zaniquelli, Hyaluronidase behavior at the air/liquid and air/lipid interfaces and improved enzymatic activity by its immobilization in a biomembrane model, J. Phys. Chem. B 115 (16) (2011) 4801–4809, http://dx.doi.org/10.1021/jp110795d.

[46] W.H. Bradley, Vertical density currents, Science 150 (3702) (1965) 1423–1428, http://dx.doi.org/10.1126/science.150.3702.1423.

[47] D.E. Graham, M.C. Phillips, Proteins at liquid interfaces: I. Kinetics of adsorption and surface denaturation, J. Colloid Interface Sci. 70 (3) (1979) 403–414, http://dx.doi.org/10.1016/0021-9797(79)90048-1.

[48] B. Keshavarzi, T. Krause, S. Sikandar, K. Schwarzenberger, K. Eckert, M.B. Ansorge-Schumacher, S. Heitkam, Protein enrichment by foam Fractionation: Experiment and modeling, Chem. Eng. Sci. 256 (2022) 117715, http://dx.doi.org/10.1016/j.ces.2022.117715.

[49] K.C. Lohfink, L. Jakob, H. Nirschl, Experimental data of continuous aqueous two-phase flotation (ATPF) with constant process parameters, 2025, http://dx.doi.org/10.35097/z9df1nhc171jm5tj, URL https://publikationen.bibliothek.kit.edu/1000179949.